AIMS Geosciences

AIMS Geosciences, 11(3): 704–724.
DOI: 10.3934/geosci.2025030
Received: 19 March 2025
Revised: 23 June 2025
Accepted: 23 June 2025
Published: 18 August 2025

https://www.aimspress.com/journal/geosciences

Research article

Comparison of machine learning techniques for thermokarst landscape mapping using Google Earth Engine

Andrei Kartoziia*

V.S. Sobolev Institute of Geology and Mineralogy, Siberian Branch of the Russian Academy of Sciences, 3 Ac. Koptug Ave., Novosibirsk, 630090, Russia

* **Correspondence:** Email: andrei.kartoziia@igm.nsc.ru; Tel: +7-383-375-0524.

Abstract: The localization of permafrost areas that are susceptible to thermokarst processes is a significant goal, given the current trend of increasing average surface temperatures in Arctic regions. The mapping of thermokarst landscapes is a significant research topic due to its relevance in understanding climate change, monitoring biodiversity, assessing carbon emissions, and informing sustainable land and water management strategies in vulnerable areas. This task can be accomplished through land cover mapping, utilizing supervised classification using machine learning techniques. In this study, we focused on comparing a range of machine learning algorithms available on the Google Earth Engine (GEE) cloud platform. We compared the performance of various models in the classification of land cover types, which relates to the degree of thermokarst process intensity. We identified that the random forest and K-nearest neighbor methods are the most effective in the classification of thermokarst landscapes, based on a visual analysis and accuracy assessment. Furthermore, we conducted the study on Arga Island (the Lena Delta). The Arga Island presents a unique opportunity for evaluating various methods of land cover mapping due to its uniformity in terms of landscape features, the monotony of deposits that make up the island, and the active thermokarst and neotectonic processes occurring there. The results obtained could be utilized in selecting the optimal model for multidisciplinary research involving various classification tasks. Additionally, the findings may be applied in future studies on landscape changes within the Lena Delta region. Furthermore, the comparison of machine learning techniques, which was conducted, may: Enhance the accuracy and efficiency of thermokarst detection; provide insights into the strengths and limitations of various algorithms; and foster the development of standardized approaches in remote sensing, which can be replicated in other studies.

Keywords: the Lena Delta; thermokarst; permafrost degradation; land cover mapping; machine learning; GEE

1. Introduction

In the past decade, all 10 of the warmest years on record have occurred [1,2]. A rising global temperature has resulted in significant changes to the Arctic ecosystems and landscape [3–5]. Global warming has led to extensive degradation of permafrost, accounting for 22% of the land area in the Northern Hemisphere [6]. The permafrost degradation leads to hazardous conditions for human life and infrastructure [7]. The processes of permafrost degradation that are activated by global warming and have an impact on Arctic ecosystems and infrastructure include thermokarst, thermal erosion, thermal abrasion, and thermal denudation [8]. To simplify the description of this study, we use the term "thermokarst" in a general sense when discussing the results of the above-mentioned processes, in accordance with [9]. Due to the potential for thermokarst to damage infrastructure and affect Arctic hydrology and ecology, mapping of thermokarst landscapes on a local and global scale in to forecast future topographical changes has become an increasingly significant task [8,10–12]. For instance, thermokarst processes may lead to topographical disturbances and the formation of depressions, which in turn may cause further thawing and degradation of the permafrost. A well-known example of a thermokarst landform is the Batagay Crater in Yakutia [13]. There are numerous instances of the impact of thermokarst on infrastructure. For example, these processes lead to the formation of thermokarst lakes [14,15], as well as landslides along the Qinghai-Tibet railway [16], which can impact the stability of infrastructure in the area. The task of mapping thermokarst landscapes on a local and global scale can be accomplished through the use of land use/land cover (LULC) mapping techniques, which utilize supervised classification methods.

LULC mapping represents a significant approach that provides invaluable insights into the utilization of land resources and the transformation of land cover (LC), which is crucial for effective planning and management purposes [17]. LC encompasses the diverse types of biological or physical cover types that exist on the Earth's surface [18]. These could include natural features such as forests, bodies of water, agricultural land, and built-up areas. LULC mapping and its derived products are extensively utilized in a diverse range of global and regional investigations across various subject areas [19,20]. Specifically, LULC maps are employed to detect alterations in Arctic landscapes and ecosystems, monitor the degradation of permafrost, and explore other impacts of global climate change [21]. For instance, the first LC dataset developed for the Arctic region is the Circum-Arctic Vegetation Map (CAVM) [22]. To date, a diverse range of global LC maps, including those covering arctic territories, are available [23,24]. Examples of successful LC mapping on a regional scale include a wide range of studies on the dynamics of thermokarst lakes [25–30].

There have also been studies detecting LC changes in Arctic regions using LULC mapping. For example, Inga Beck and colleagues [31] used high-resolution remote sensing imagery and four Landsat images, as well as ground-based data, to estimate land cover changes within the extent of discontinuous permafrost, which strongly affects the forest-tundra ecotone in northern Quebec, Canada. They conducted post-classification analysis based on two independently generated spectral classification results from two dates. This was followed by a pixel-by-pixel comparison to detect any changes in land cover type. As a result, they identified the dynamics of vegetation cover and water bodies between

1986 and 2009. Julia Boike et al. [32] analyzed MODIS-derived NASA products and two mosaics of Landsat satellite images to identify land cover changes in central Yakutia between 2000 and 2011. They focused on studying water bodies, land surface temperatures, leaf area index, the occurrence and extent of forest fires and the area, and duration of snow cover. Consequently, the land cover mapping enabled the authors to observe a warming trend and identify a complex interaction between various mechanisms affecting land cover and surface temperatures. Yeji Lee and colleagues [33] analyzed land cover changes in central Yakutia over a 19-year period from 2001 to 2019 using sparse time series Landsat data. The implementation of complex methods, including the identification of short- and long-term classes within the study area and their dynamics, enabled the authors to characterize patterns of land cover change. Nitze et al. [34] provided another example of the successful use of land cover mapping to estimate changes in permafrost landscapes. They analyzed the Landsat time-series imagery from 1999 to 2014 for four continental-scale transects in order to quantify the abundance and distribution of disturbances in the permafrost regions. Therefore, there have been numerous researchers that have focused on LULC mapping in regions with permafrost. These studies have demonstrated the diverse range of data sources and methods used to identify changes in land cover. Comparing mapping techniques and determining the most effective method depends on the specific data, study area, and research objectives is an important task today.

The recent advances in LULC mapping would not be possible without the vast amount of remote sensing (RS) data collected, the development of cloud-based platforms, and the use of machine learning (ML) algorithms [35]. Today, researchers have access to a large number of images from Landsat and Sentinel satellite missions. The commencement of additional satellite missions has led to improvements in the spectral, spatial, and temporal resolution of the satellite imagery, which enables the analysis trends in LC change [11]. Moreover, the application of machine learning techniques for mapping has gained prominence, resulting in improved precision in the mapping process [11,21]. These methods rely on data-driven learning and decision-making with minimal human intervention. The emergence of the Google Earth Engine (GEE) platform has led to a significant shift in the approach to remote sensing [36]. The GEE is a free cloud-based platform that provides access to RS data, enabling users to analyze it using a range of ML techniques [20,37]. Therefore, the use of GEE platforms enables not only the analysis of RS data, but also the comparison of the ML algorithms performance in LC mapping.

The evaluation of ML classifier performance has been enabled by the use of cloud computing, and such assessments have become a relevant area of research. Generally, the visual method for interpreting RS data and inspecting classification results is a conventional approach that provides a reasonable assessment of model performance [38]. However, this method is not applicable to large areas and often depends on the professional skills of the researchers. Therefore, the performance of classifiers in LC mapping is statistically estimated through validation and accuracy assessment techniques. Statistical estimates of model performance are provided by accuracy metrics, which are calculated based on a confusion matrix. In turn, this matrix is generated by comparing the classified values with those in the validation dataset. A number of studies have been conducted to evaluate the performance of ML models for LULC mapping [39]. For example, Zhewen Zhao and colleagues compared land use and land cover (LULC) maps of the Mardan city (Pakistan, Khyber Pakhtunkhwa province), which were generated using three ML algorithms [40]. Additionally, K.S. Rawat and co-authors [41] compared the performance of three ML algorithms in the LULC mapping of a city area. Anam Nigar and colleagues [42] conducted a more in-depth study comparing ML and deep learning methods for

land classification. Similarly, to the aforementioned studies, we aim to evaluate the effectiveness of machine learning algorithms in land cover mapping. However, we focused on mapping thermokarst terrains.

Therefore, our main objective of this study is to identify the optimal ML model for land cover classification in thermokarst terrains using the GEE platform. To achieve this goal, we performed the following steps. The first step was to create a dataset, which involved filtering satellite imagery and computing indices. Then, we identified LC classes and prepared training samples. After that, we divided these samples into two sets: One for training and one for subsequent validation. The second stage involved the supervised classification of composite using six ML models: Classification and regression trees, gradient tree boosting, random forests, k-nearest neighbors, support vector machines, and minimum distance classifiers. We selected optimal hyperparameter values through their tuning and estimation of the overall accuracy of classifiers. Ultimately, we determined the optimal hyperparameters for each classifier, under which they achieved the best performance. The final stage of the study involved a comprehensive evaluation of the classifier's performance using a range of accuracy metrics. We calculated the following metrics based on the confusion matrix: Recall, precision, F1 score, overall accuracy, kappa coefficient, and classification success index. Finally, we compared the classifiers based on these calculated metrics and visual analysis.

2. Materials and methods

2.1. Study area

The analyzed area is in the northwestern part of the Lena Delta, occupying the central part of Arga Island (Figure 1). It covers approximately 2,000 square kilometers. The Lena Delta is comprised of three terraces, each with its own unique geomorphic and sedimentary features, as well as distinct ages [43,44]. Arga Island is traditionally associated with the second one. The elevation of the island varies from 10 to 30 meters above sea level (a. s. l.). The depth of the permafrost in this region ranges from 400 to 1000 m [45]. A massive cryostructure is a typical feature of Arga Island sedimentary deposits [46]. The active layer is about 20 to 40 cm deep. According to the latest detailed analysis of Lena Delta's climate conditions [47], the average monthly air temperature for the coldest month was −32.7 °C (−25.6 °F), while the average monthly temperature for the warmest month was 9.5 °C (48.2 °F). In recent years, the average annual surface temperature has increased in the Laptev Sea region and in the Lena Delta, leading to areas of hydrological changes. This has been demonstrated by numerous observations [47–49].

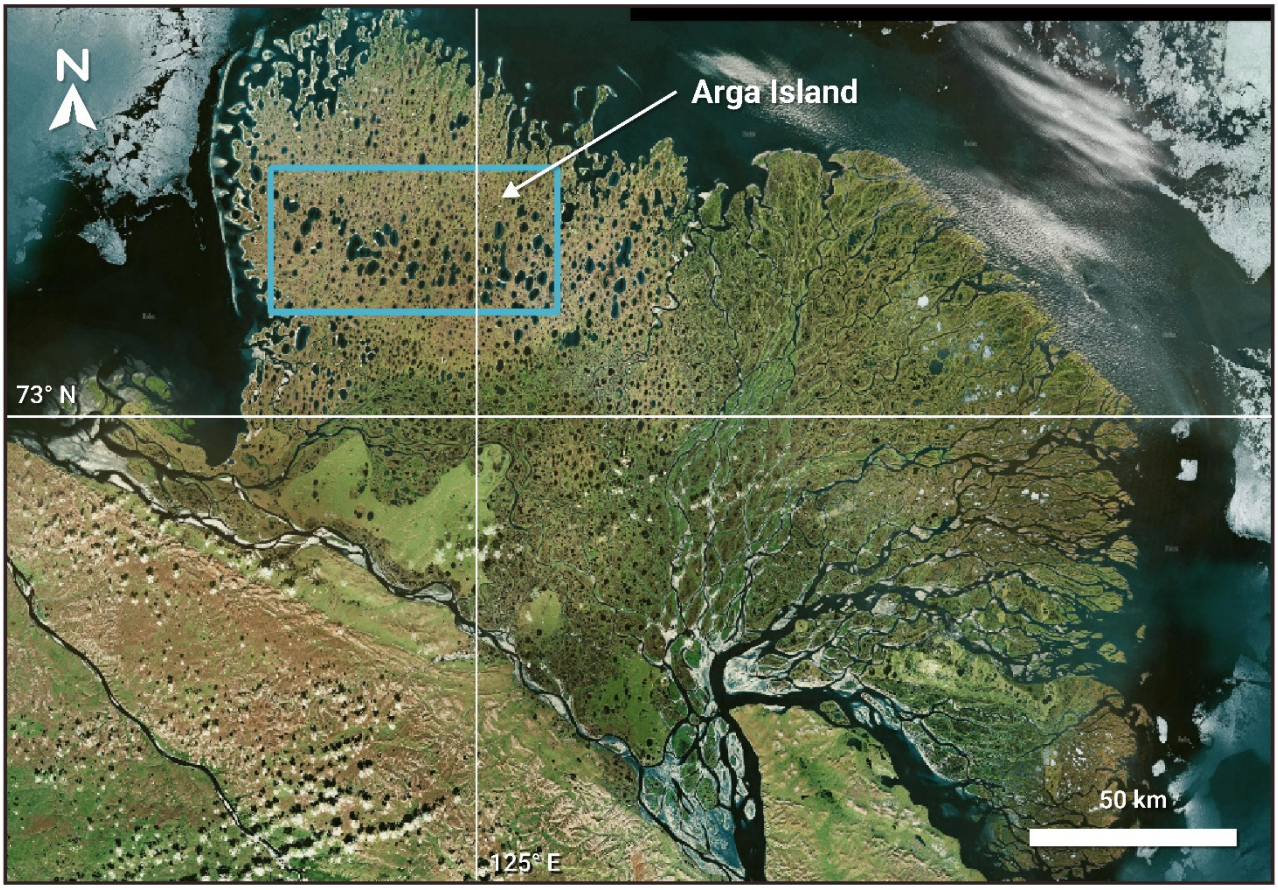

Figure 1. The location of the study area is indicated by the blue rectangle in the satellite image of the Lena Delta.

The Arga Island is known for its uniform pattern of thermokarst topography. There are thermo-erosional valleys and thermokarst depressions on the entire island surface. Thermokarst depressions typically contain sub-meridional thermokarst lakes within their central parts [46,50]. The deposits on the island are composed of fluvial sediments with a fine grain size and no silt, clay, or organic material throughout the area [51]. The uniformity of landscape features simplifies the LC mapping process by reducing the number of LC classes that need to be considered. It has also been noted that the Lena Delta is affected by active tectonic processes [43,45,52–55]. These processes have an impact on the permafrost degradation and the landscape dynamic. Therefore, the aforementioned features make Arga Island a unique test site for identifying previously undiscovered patterns of periglacial landscape transformations and for testing methods for LC mapping of thermokarst terrains.

2.2. Data processing and mapped LC classes

All research was conducted on the GEE platform, which included image processing, collection of training samples, supervised classification, and analysis of the performance of ML models. We selected the image from Sentinel-2 for our analysis over other satellite imagery due to its superior spatial resolution of 10 meters, its more frequent revisit frequency of every 5 days, its broader spectral

coverage, including red-edge and short-wave infrared bands, and its free availability. These factors make Sentinel-2 images a more appropriate choice for our research into the development of Arctic landscape monitoring techniques. As our main objective of the study was to compare the results of various classification methods for the first time in the region under investigation, it was crucial to select a cloud-free image taken during the summer season, when there was no snow and peak vegetation activity was present. Initially, we selected the most appropriate Sentinel-2 image (Level-2A) from the summer period by filtering and sorting based on cloud coverage. This image was captured on 29th July 2021, with a cloud coverage of 0.008006% of the pixels. The details of the Sentinel-2 bands are provided in Table 1.

Table 1. The band characteristics of Sentinel-2 satellite imagery [56].

Band	Pixel Size (m)	Central Wavelength (nm)	Description
B1	60	442.3	Aerosols
B2	10	492.1	Blue
B3	10	559	Green
B4	10	665	Red
B5	20	703.8	Red Edge 1
B6	20	739.1	Red Edge 2
B7	20	779.7	Red Edge 3
B8	10	833	NIR
B8A	20	864	Red Edge 4
B9	60	943.2	Water vapor
B11	20	1610.4	SWIR 1
B12	20	2185.7	SWIR 2

We added spectral indices to provide additional information for the classifiers and improve classification results. All these indices were chosen because they are widely used for estimating biomass and identifying water bodies that are primarily affected by thermokarst processes. We used the Normalized Difference Vegetation Index (NDVI) [57], the Normalized Difference Water Index (NDWI) [58], the Enhanced Vegetation Index (EVI) [59], and the results of the Tasselled Cap transformation, wetness (TCW) and greenness (TCG) [60,61]. The NDVI is a widely used spectral index for assessing the health of plant cover. We incorporated the EVI, which enhances the ability to detect changes in vegetation and complements the information provided by the NDVI [59]. On the other hand, the use of the TCG approach provides a more detailed understanding of vegetation dynamics, as it can differentiate between various aspects of vegetation reflectance [62]. We employed the NDWI and the TCW as indicators of water surface presence and soil moisture conditions. Therefore, the selected spectral indices comprehensively describe the biomass and hydrologic characteristics of the study area. The formulas of the indices are presented in Table 2. Furthermore, after indices calculation and normalizing the initial Sentinel-2 image bands, we used principal components analysis (PCA) to derive new uncorrelated bands from the dataset. We selected the first three PCA results, normalized them, and added them to the dataset. Therefore, the final dataset comprises normalized Sentinel-2 Level-2A bands (B1-B12), calculated indices (NDVI, NDWI, EVI, TCW, and TCG), and the three PCA results (PCA 1, PCA 2, and PCA 3).

Table 2. The used spectral indices. The band's names in the formulas are in accordance with Table 1.

Index	References	Formula
NDVI	[57]	(B8 − B4)/(B8 + B4)
NDWI	[58]	(B3 − B8)/(B3 + B8)
EVI	[59]	2.5 × (B8 − B4)/((B8 + 6.0 × B4 − 7.5 × B2) + 1.0)
TCW	[60,61]	0.1509 × B2 + 0.1973 × B3 + 0.3279 × B4 + 0.3406 × B8 + 0.7112 × B11 + 0.4572 × B12
TCG	[60,61]	−0.2848 × B2 − 0.2435 × B3 − 0.5436 × B4 + 0.7243 × B8 + 0.0840 × B11 − 0.1800 × B12

There are various classifications of thermokarst landforms and stages of their appearances [8,9]. We established five LC classes through a review of the literature and a visual examination of the study region, utilizing RS data. Moreover, we generally streamlined the classification of thermokarst landscapes and identified common categories that can be specifically related to the degree of permafrost degradation. We have provided a list of all LC classes in Table 3 and Figure 2. The detailed description of the mapped LC classes, including visual examples and justifications for differences in their spectral characteristics, is presented in another study [63].

We identified 20 training data polygons per LC class, which were distributed evenly across the study area. The final dataset comprised 100,805 sample points with unique values. These were randomly split into two categories: Training (61%) and validation (39%).

Table 3. Description of mapped LC classes.

LC class	Class ID	Description
Water bodies	1	All water bodies, ranging from small ponds to large elongated thermokarst lakes, as well as the water surfaces of streams.
Stable terrains	2	Stable areas with lighter and more yellowish tones in true color imagery. Training polygons for this class were mapped on flat upland surfaces unaffected by intense thermokarst processes.
Thermokarst-affected terrains	3	Areas affected by intense thermokarst processes with a darker and more brownish tone in the true color band combination. Training polygons for the thermokarst-affected terrain were mapped in the bottoms of the thermokarst hollows and erosion valleys.
Slopes	4	Greyish areas in a true color band combination, which surround thermokarst hollows or are located along streams.
Blowouts	5	A specific class for blowouts that significantly differ from other classes. They were added to the LC map as an independent class to avoid mistakes in ML models.

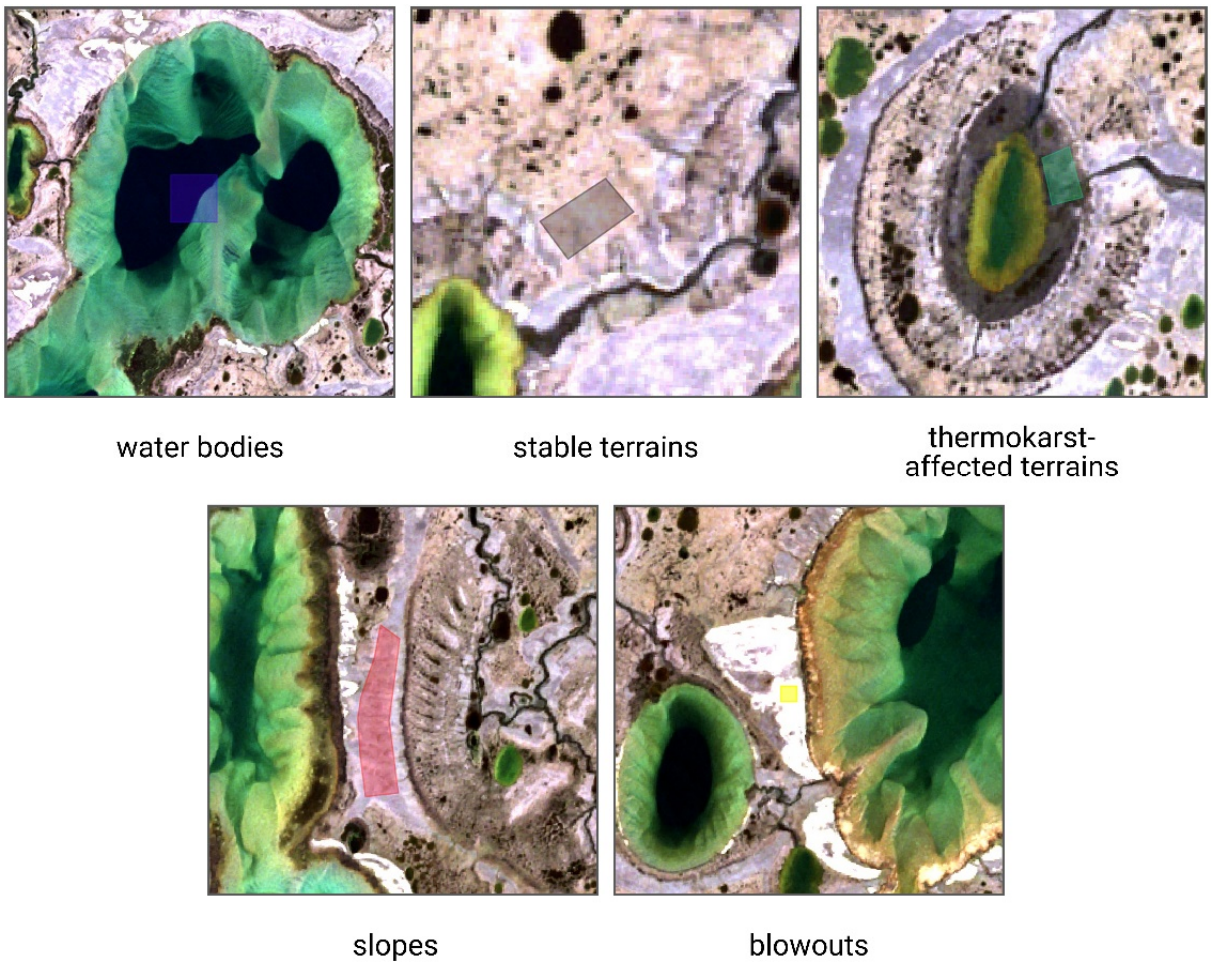

Figure 2. The examples of five mapped LC classes with corresponding training polygon contours.

2.3. Models

The GEE platform makes it possible to utilize a range of machine learning techniques that are commonly used for LULC mapping. Based on our objectives, we compared the outcomes of several popular ML algorithms. These were classification and regression trees, gradient tree boosting, random forests, k-nearest neighbors, support vector machines, and minimum distance classifiers.

The comparison process can be described as follows. Initially, we processed the data and generated a training and validation set as described above. Then, we trained one of the ML models with various hyperparameters. Due to the GEE's capacity for analyzing large volumes of data, it is possible to analyze several variants of the model that have been trained with different hyperparameters. Then, we performed supervised classification of the study area and evaluated the overall accuracy of each model variant. Following this, we identified a combination of hyperparameters for the model that enabled it to achieve the best performance. In the next phase, we tested other ML models and determined the optimal combination of hyperparameters for each one. As a result, we obtained six ML models that demonstrated the best performance. These models were used for further comparison of ML techniques. Below is a brief description of each model and its hyperparameters.

The classification and regression trees (CART) method is a variant of the decision tree algorithm that can handle both classification and regression tasks [64]. CART constructs a tree-like structure consisting of nodes and branches. The terminal nodes in the tree contain a predicted category label or value for the target variable. We did not impose any restrictions on the values of the maximum number of nodes or the minimum leaf population in this model.

Gradient tree boost (GTB) constructs trees one at a time [65]. Each new tree is designed to correct the errors or deficiencies of the existing collection of trees. The trees employed in GBT are typically decision trees, which are created by dividing the input space (features) in a manner that minimizes a predetermined loss function. After each tree is integrated into the model, the algorithm calculates the loss function, which measures the discrepancy between the current ensemble's predictions and the actual values. The differences between the predicted and actual values are then used to construct the subsequent tree. The model achieved the best outcome with 6 trees.

The random forest (RF) algorithm is a machine learning technique that creates multiple decision trees during training and produces the most frequent class label for classification or the average prediction value for regression [66]. Each tree in the random forest model is constructed using a random selection of features and a subset of the training data. The final prediction is derived by combining the results of all individual trees in the ensemble. The RF algorithm demonstrated the highest overall accuracy when the number of trees was set to 110.

The k-nearest neighbor (KNN) algorithm is a non-parametric supervised learning classifier that uses proximity to make predictions [67]. This model works by identifying the k-nearest neighbors of a given data point, based on a specific distance metric. In this study, the KNN algorithm demonstrated the best performance when using k = 7 and the Manhattan distance metric.

The support vector machine (SVM) algorithm separates two categories by locating the ideal boundary that maximizes the distance between the closest data points of opposite categories [68]. The number of features in the input data determines whether the boundary is a line in a two-dimensional space or a plane in a multi-dimensional space. Since there can be multiple boundaries that separate categories, maximizing the distance between points enables the algorithm to find the best boundary between categories. The lines that are adjacent to the ideal boundary are known as support vectors, as these vectors pass through the data points that determine the maximum distance. We used an SVM model with a C parameter of one.

The minimum distance (MIND) classifier determines the distance between a pixel's value and the mean value for each class and assigns the pixel to the class that has the smallest distance. The MIND algorithm demonstrated the best performance when using the cosine distance metric in the presented study.

2.4. Accuracy assessment

Following the training of the classifier and the classification of the dataset, we compared the predicted values with those in the validation set using the ee.Classifier.confusionMatrix() method. Thus, we calculated a confusion matrix (CM) for each model. Then, we calculated the following metrics based on the CM for a comprehensive quantitative assessment of model performance. The primary metric, overall accuracy (OA), was derived by dividing the sum of true positive and true negative classifications by the total data points [69,70]. Recall (producer's accuracy, PA) was calculated by dividing correctly classified pixels in a class by the total pixels in that class [69,70]. Precision (consumer's accuracy, CA) was determined by dividing true positive pixels by the total pixels

predicted for the class [69,70]. The F1 score was computed as the harmonic mean of precision and recall [71]. The Kappa coefficient, which evaluates consistency across variable measurements under different conditions, was used to assess classification accuracy against random assignment [72]. Additionally, the classification success index (CSI), a class-specific symmetric measure, was calculated as the sum of recall and precision minus one [73,74].

3. Results and discussion

3.1. Classification results

We generated the LC map of the study area using ML models. The results are presented in Table 4 and Figure 3. The spatial distribution of the mapped LC classes illustrates how different models statistically tend to categorize pixels. The CART model classified a greater number of water bodies compared to other models. RF and KNN models do not have any maximum or minimum values. Although the RF model mapped a larger number of pixels of thermokarst-affected terrain, KNN categorized a greater number of pixels as stable terrain and slopes. The SVM model tends to map thermokarst-affected terrains and slopes, but it has classified a minimum number of pixels as stable areas. Conversely, the MIND model categorized a greater number of pixels as stable terrains. However, this model mapped a significantly smaller number of pixels to thermokarst-affected terrains. Given that the outcome of the MIND model demonstrates extreme values in the two most significant classes compared to other models, the accuracy of this model is doubtful.

Table 4. The area of LC classes (in km²), as determined by various models.

Models	water bodies	stable terrains	thermokarst-affected terrains	slopes	blowouts
CART	423.89	550.41	672.51	316.14	28.92
GTB	406.06	538.37	693.36	318.77	35.31
RF	397.98	539.35	716.15	308.42	29.97
KNN	392.02	567.96	673.05	330.94	27.92
SVM	394.29	513.02	717.70	342.25	24.62
MIND	384.77	744.61	504.19	341.86	16.45

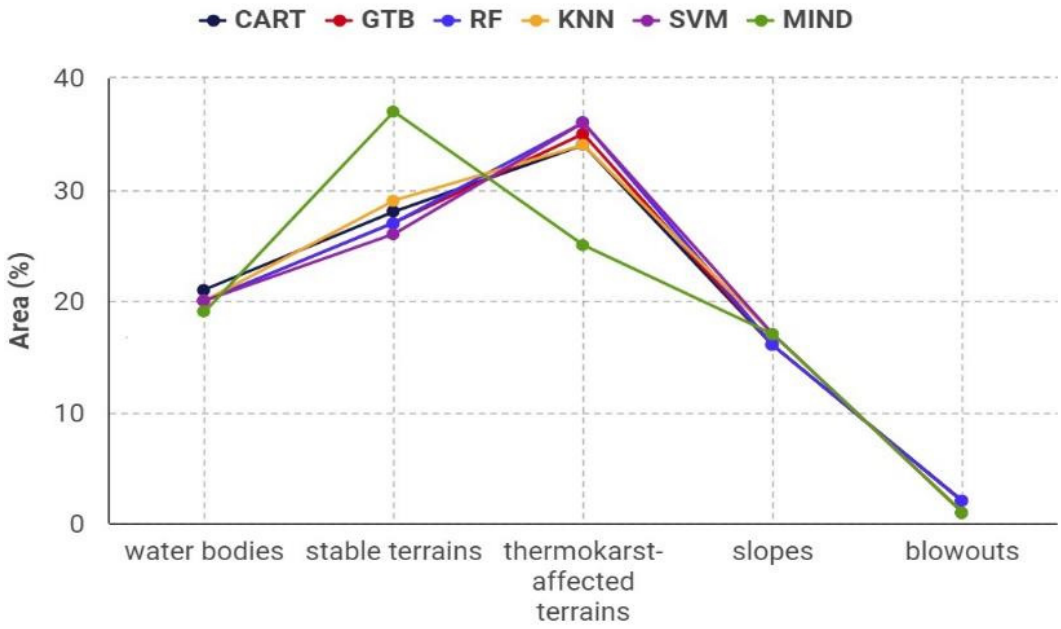

Figure 3. The spatial distribution of LC classes in percentage.

3.2. Performance Evaluation

3.2.1. Visual inspection of ML model performance

Initially, we visually analyzed the results of the ML models. The inspection of the results involved visually interpreting some parts of the study area [75]. After visually recognizing the LC class, we compared it with the classification outcomes. This step enabled us to identify gross errors of the classifiers and determine which algorithms evidently failed to perform the task. The visual inspection indicated the following.

All classifiers experienced difficulties with pixels at the boundaries between classes. This was due to the fact that these pixels often exhibit intermediate spectral properties and may therefore be classified as belonging to either category. Additionally, the classifiers made some mistakes in the categorization of small, shallow water bodies, thermokarst-affected terrains, and stable terrains. The pixels of these categories frequently have similar spectral properties.

The visual inspection revealed that the two classifiers, CART and GTB, exhibited critical errors in water body recognition (Figure 4a). Apparently, this was due to the peculiarities of the algorithms themselves. The MIND classifier was observed to make errors in distinguishing stable and thermokarst-affected terrain. As a result, it often misclassified thermokarst-affected terrains as stable terrains (Figure 4b). The SVM model had difficulty recognizing blowouts and frequently misclassified small, shallow water bodies as thermokarst-affected terrains (Figure 4b). The KNN and RF models generated similar and, as far as possible, visually satisfactory results (Figure 4c). The results of all six models for the same area are also shown in Figure 5.

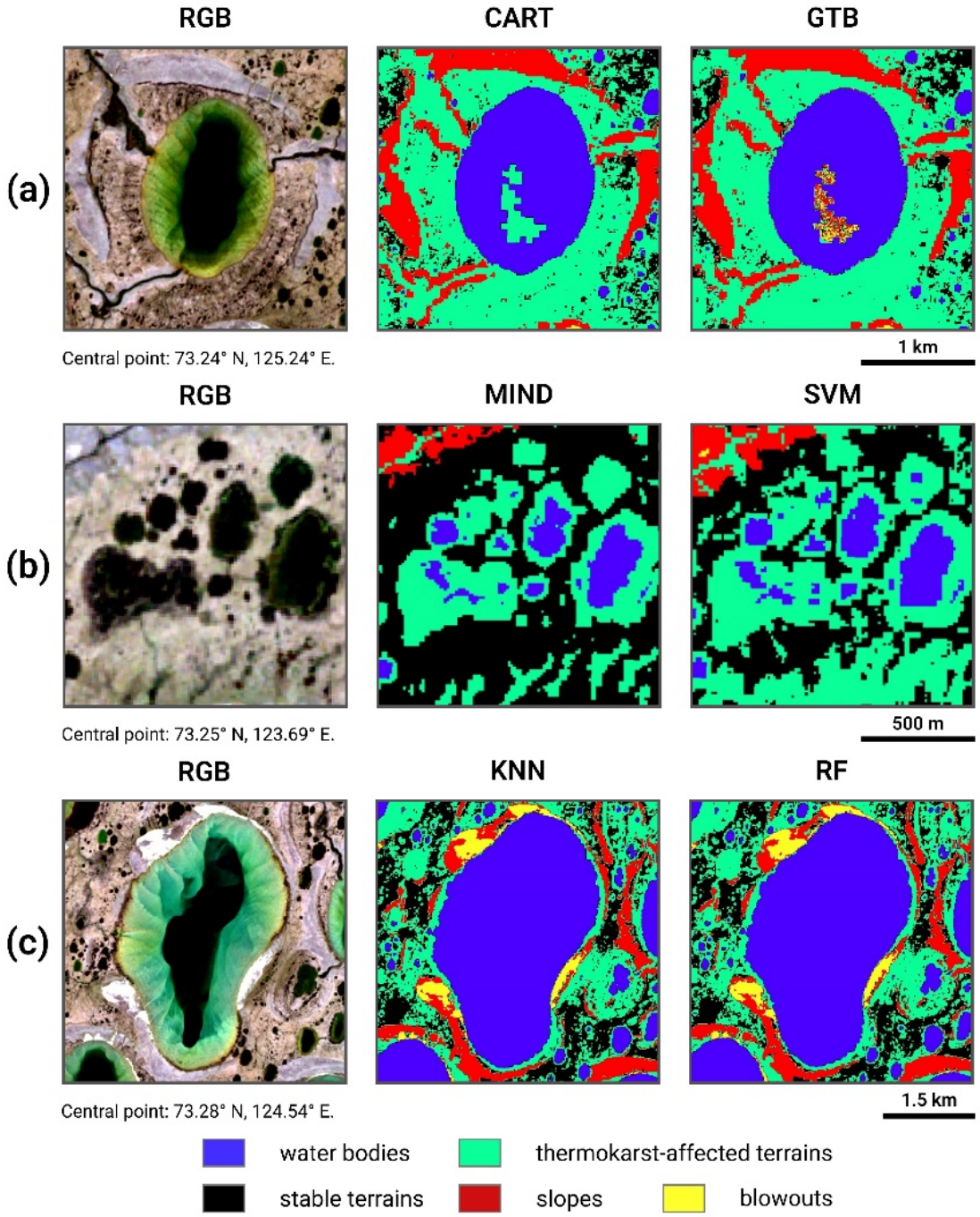

Figure 4. Visual inspection of ML models performance: (a) Critical errors of the CART and GTB algorithms in water body recognition; (b) errors in the classification of sable terrains, thermokarst-affected terrains, and water bodies by MIND and SVM; and (c) the fragments of the LC classes' distribution maps, which were created using the KNN and RF techniques.

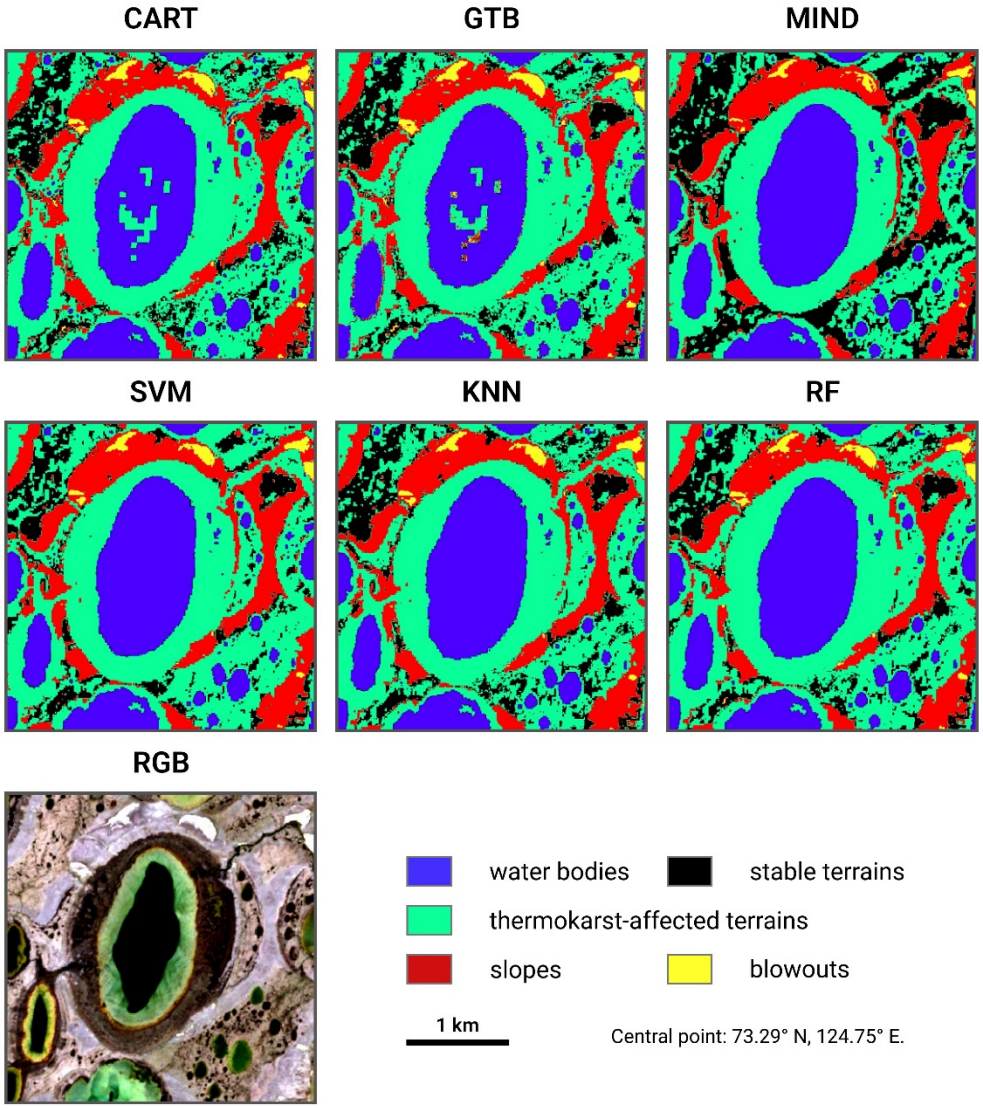

Figure 5. The fragments of the LC classification maps, which were generated using all the compared ML techniques.

3.2.2. Accuracy assessment

Based on the above-mentioned methods, we generated CM for all ML models in order to conduct an accuracy assessment. We further calculated the following metrics: Recall, precision, F1 score, Kappa, classification success index (CSI), and overall accuracy (OA) (Figure 6, Table 5). The quality assessment results suggested that, on average, the CART, GTB, SVM, and MIND classifier performances are statistically inferior compared to those of RF and KNN models.

It should be noted that there were some features in the classification of certain LC classes. For instance, some classifiers demonstrated better recall and lower precision metrics for certain classes. This means that the model correctly classified actual pixels that belong to this class, as well as pixels from other classes that were also assigned to this class. The RF model demonstrated this by classifying

water bodies and stable terrains. In contrast, KNN and SVM models exhibit superior recall performance for thermokarst-affected terrains, slopes, and blowouts.

Likewise, models could demonstrate higher precision metric and lower recall. In this case, classifiers skipped some pixels that belong to a class, but it can be assured that pixels that are classified as belonging to that class do concern to that class. The RF model showed this during the classification of thermokarst-affected terrain, slopes, and blowouts. Moreover, SVM and MIND models demonstrated superior precision in the classification of water bodies. Overall, these models are the most effective in identifying this class.

The F1 score and CSI metrics produced similar results in assessing the accuracy of ML models. These metrics indicated that RF and KNN models performed well, without significant failures in classifying certain classes. The kappa statistic demonstrated that the results of the RF and KNN algorithms differed as much as possible from random LC class recognition. The overall accuracy of these models was also the highest among the classifiers compared. Therefore, we can assume that RF and KNN are generally the most effective methods in our classification task. However, the RF model is more accurate in classifying thermokarst-affected terrains. In the case of RF, we can have more confidence that pixels related to this important class belong to it.

a) Recall (%)

Class	CART	GTB	RF	KNN	SVM	MIND
1	98.43	98.35	99.16	98.8	98.67	98.52
2	94.81	95.49	99.38	96.43	93.52	97.58
3	98.63	98.51	96.31	98.89	99.3	96.98
4	97.27	98.83	98.36	99.29	99.16	97.16
5	99.97	100	99.98	100	100	99.92
Average	97.82	98.24	98.64	98.68	98.13	98.03

b) Precision (%)

Class	CART	GTB	RF	KNN	SVM	MIND
1	99.03	98.85	98.92	99.43	99.93	99.92
2	98.9	99.07	96.1	99.11	99.45	95.14
3	93.71	95.51	99.02	96.44	94.02	98.23
4	97.75	98.04	99.11	98.45	97.51	97.04
5	99.89	99.77	100	100	100	100
Average	97.86	98.25	98.63	98.69	98.18	98.07

c) F1 score (%)

Class	CART	GTB	RF	KNN	SVM	MIND
1	98.73	98.6	99.04	99.11	99.29	99.21
2	96.81	97.25	97.71	97.75	96.39	96.35
3	96.11	96.98	97.65	97.65	96.59	97.6
4	97.51	98.43	98.73	98.87	98.33	97.1
5	99.93	99.88	99.99	100	100	99.96
Average	97.82	98.23	98.62	98.68	98.12	98.04

d) classification success index (%)

Class	CART	GTB	RF	KNN	SVM	MIND
1	97.47	97.2	98.08	98.23	98.6	98.44
2	93.71	94.56	95.48	95.54	92.97	92.73
3	92.34	94.01	95.33	95.33	93.32	95.2
4	95.02	96.87	97.47	97.74	96.67	94.2
5	99.86	99.77	99.98	100	100	99.92
Average	95.68	96.48	97.27	97.37	96.31	96.10

Figure 6. The quality validation results of classification for each LC class.

Table 5. The accuracy assessment metrics of ML models (in %).

Models	Recall	Precision	F1 Score	CSI	Kappa	OA
CART	97.82	97.86	97.82	95.68	97.26	97.81
GTB	98.24	98.25	98.23	96.48	97.79	98.23
RF	98.64	98.63	98.62	97.27	98.28	98.62
KNN	98.68	98.69	98.68	97.37	98.34	98.67
SVM	98.13	98.18	98.12	96.31	97.65	98.12
MIND	98.03	98.07	98.04	96.1	97.54	98.03

3.3. Discussion

Based on the research, we found that the RF model is the most effective classifier for the given classification task. This finding is in line with a number of other studies, which also reported the successful performance of this algorithm [76–78]. One of the key reasons for the success of this algorithm is the combination of multiple decision trees into a single model. This aggregation of predictions from multiple trees helps to improve the model accuracy, especially in the classification of pixels with an uncertain spectral signature.

The KNN algorithm has also demonstrated high accuracy due to the balanced training data and the local analyzed region, which has a monotonous landscape. Owing to this, pixels can be successfully classified based on their distance to the training points in the feature space. However, it is difficult to recommend the use of this algorithm for LC classification in thermokarst areas in other regions, given the features of the KNN model. For example, KNN has limitations when dealing with large datasets, specifically in terms of its computational efficiency and scalability.

It is important to note the significance of visual analysis of classifier outputs in addition to statistical assessment of model performance. Often, researchers present only statistical estimates of classifier accuracies. Nevertheless, visual estimation can help identify critical errors of classifiers and make detailed analysis of numerical metrics for classifier accuracy meaningless; this is especially so during comparisons of the ML model's performance in classifying different LC classes.

We conducted a comparison of different ML models to determine the best algorithm for supervised classification of LC classes related to thermokarst intensity. We intend to utilize the findings of the RF algorithm in future research. For example, we intend to utilize this classification outcome in the development of a method for identifying areas of permafrost that are susceptible to intense thermokarst processes. In addition, we plan to utilize this ML model in the detection of temporal dynamics of LC classes on the Arga Island. This detection will enable the completion and continuation of previous research on the dynamics of the landscape in the Lena Delta region [79].

Therefore, our findings of this study represent a starting point for the development of a comprehensive method to analyze and monitor thermokarst landscapes and their responses to global warming. The recognition of the described land cover classes in the time series of satellite imagery will enable the quantitative estimation of landscape changes over time. This, in turn, would enable the identification of certain aspects of the interactions between hydrology, vegetation, and geomorphological characteristics of the Arctic lowlands. Finally, the acquired information will be utilized for modeling future changes in ground characteristics, their impact on infrastructure, and policy-making regarding development in Arctic regions. Furthermore, quantitative estimates of

landscape changes can provide a basis for an adequate and clear understanding of natural alterations under global warming and eliminate the influence of subjective assessments and political interference.

4. Conclusions

The significance of LC mapping cannot be overstated in the context of sustainable development. ML algorithms have produced dependable, precise, and trustworthy LC classification results. By comprehending the factors that affect the accuracy of the algorithm, we can enhance the classification outcomes. In this study, we identified the optimal ML model for LC classification in thermokarst terrains using the GEE platform.

Based on the comparison conducted, we determined that the RF model is the most effective classifier for the specified classification task among the algorithms available on the GEE platform. However, the KNN model does not significantly differ in accuracy and can also be used for local studies of thermokarst landscapes. These two classifiers are statistically the most accurate models based on the accuracy assessment. The analysis of accuracy metrics enabled us to identify the models that showed the best performance in classifying LC classes. Moreover, it is worth noting the significance of visual analysis of classification results: Due to the visual assessment carried out, we identified that the CART and GTB models made critical errors in classification.

The presented results could therefore be useful in future studies of thermokarst landscapes. Specifically, we can identify some areas for further research based on this study. The first direction is to clarify the presented findings and determine the limitations of the two best ML algorithms (RF and KNN). This could involve exploring the performance of the model across other geomorphological surfaces in the Lena Delta, as well as in classifying several satellite imagery from different times and in varying environmental conditions, such as cloud cover and seasonal variations. The second area of application for the presented results is in multidisciplinary research, as the mapped LC classes represent a wide range of landscape components within the study area. The classification results can provide information on hydrological conditions, soils, and vegetation cover of the territory. Accordingly, they can be utilized in various multidisciplinary studies. Furthermore, the comparison conducted has answered the question of which ML model can be employed in studies with different classification tasks. With regard to our specific plans, we will use the classification results from the RF model to identify areas that are susceptible to thermokarst processes. Furthermore, we intend to utilize the RF model to monitor the dynamics of the landscape in the Lena Delta region. It should also be noted that the developed methods for thermokarst landscape monitoring can be applied to other regions of the Arctic lowlands and can be repeated using other remote sensing platforms.

Use of AI tools declaration

The authors declare they have not used Artificial Intelligence (AI) tools in the creation of this article.

Acknowledgments

This research was funded by the Russian Science Foundation (Project #23-77-01029 https://rscf.ru/en/project/23-77-01029/). The classification success index was calculated and analyzed under the state assignment of IGM SB RAS (№122041400252-1). The author is grateful to his teacher,

Ivan Zolnikov, and the administration of the IGM SB RAS for their help and encouragement. We would like to thank two anonymous reviewers for their valuable comments and suggestions, which have significantly improved the manuscript.

Conflict of interest

The author declares no conflicts of interest.

References

1. Lee H, Calvin K, Dasgupta D, et al. (2023) Climate Change 2023: Synthesis Report. Contribution of Working Groups I, II and III to the Sixth Assessment Report of the Intergovernmental Panel on Climate Change.
2. Wang L, Wang L, Li Y, et al. (2023) A century-long analysis of global warming and earth temperature using a random walk with drift approach. *Decis Anal J* 7: 100237. https://doi.org/10.1016/j.dajour.2023.100237
3. Serreze M, Barrett A, Stroeve J, et al. (2009) The emergence of surface-based Arctic amplification. *Cryosphere* 3: 11–19. https://doi.org/10.5194/tc-3-11-2009
4. Cohen J, Screen JA, Furtado J, et al. (2014) Recent Arctic amplification and extreme mid-latitude weather. *Nat Geosci* 7: 627–637. https://doi.org/10.1038/ngeo2234
5. Jansen E, Christensen J, Dokken T, et al. (2020) Past perspectives on the present era of abrupt Arctic climate change. *Nat Clim Change* 10: 714–721. https://doi.org/10.1038/s41558-020-0860-7
6. Obu J, Westermann S, Bartsch A, et al. (2019) Northern Hemisphere permafrost map based on TTOP modelling for 2000–2016 at 1 km^2 scale. *Earth-Sci Rev* 193: 299–316. https://doi.org/10.1016/j.earscirev.2019.04.023
7. Streletskiy D, Anisimov O, Vasiliev A (2015) Chapter 10 - Permafrost Degradation, In: Shroder JF, Haeberli W, Whiteman C (Eds.), *Snow and Ice-Related Hazards, Risks, and Disasters*, Boston, Academic Press, 303–344. https://doi.org/10.1016/B978-0-12-394849-6.00010-X
8. French H (2017) *The periglacial environment*, Hoboken, NJ, Wiley, Blackwell, 560.
9. Jorgenson M (2013) 8.20 Thermokarst Terrains, In: Shroder JF (Ed.), Treatise on Geomorphology, San Diego: Academic Press, 313–324. https://doi.org/10.1016/B978-0-12-374739-6.00215-3
10. Jorgenson M, Grosse G (2016) Remote Sensing of Landscape Change in Permafrost Regions. *Permafrost Periglacial Processes* 27: 324–338. https://doi.org/10.1002/ppp.1914
11. Philipp M, Dietz A, Buchelt S, et al. (2021) Trends in Satellite Earth Observation for Permafrost Related Analyses—A Review. *Remote Sens* 13. https://doi.org/10.3390/rs13061217
12. Chen Y, Liu A, Cheng X (2022) Landsat-Based Monitoring of Landscape Dynamics in Arctic Permafrost Region. *J Remote Sens*, 9765087. https://doi.org/10.34133/2022/9765087
13. Kizyakov AI, Wetterich S, Günther F, et al. (2023) Landforms and degradation pattern of the Batagay thaw slump, Northeastern Siberia. *Geomorphology* 420: 108501. https://doi.org/10.1016/j.geomorph.2022.108501
14. Zhu J, Luo J, Zhang H, et al. (2024) Distribution and changes of thermokarst lakes along the Qinghai-Tibet Railway from 1991 to 2022. *Res Cold Arid Reg*. https://doi.org/10.1016/j.rcar.2024.10.005
15. Zhou G, Liu W, Xie C, et al. (2024) Accelerating thermokarst lake changes on the Qinghai–Tibetan Plateau. *Sci Rep* 14: 2985. https://doi.org/10.1038/s41598-024-52558-7

16. Wei T, Wang H, Cui P, et al. (2024) Formation and evolution of thermokarst landslides in the Qinghai-Tibet Plateau, China. *Sci Total Environ* 954: 176557. https://doi.org/10.1016/j.scitotenv.2024.176557
17. Turner B, Lambin E, Reenberg A (2007) The emergence of land change science for global environmental change and sustainability. *Proc Natl Acad Sci* 104: 20666–20671. https://doi.org/10.1073/pnas.0704119104
18. Jansen L, Di Gregorio A (2000) *Land Cover Classification System (LCCS): Classification Concepts and User Manual*, Rome: Food and Agriculture Organization of the United Nations, 79.
19. Nedd R, Light K, Owens M, et al. (2021) A Synthesis of Land Use/Land Cover Studies: Definitions, Classification Systems, Meta-Studies, Challenges and Knowledge Gaps on a Global Landscape. *Land* 10, 994. https://doi.org/10.3390/land10090994
20. Zhao Q, Yu L, Li X, et al. (2021) Progress and Trends in the Application of Google Earth and Google Earth Engine. *Remote Sens* 13, 3778. https://doi.org/10.3390/rs13183778
21. Beamish A, Raynolds M, Epstein H, et al. (2020) Recent trends and remaining challenges for optical remote sensing of Arctic tundra vegetation: A review and outlook. *Remote Sens Environ* 246: 111872. https://doi.org/10.1016/j.rse.2020.111872
22. Walker D, Gould W, Maier H, et al. (2002) The Circumpolar Arctic Vegetation Map: AVHRR-derived base maps, environmental controls, and integrated mapping procedures. *Int J Remote Sens* 23: 4551–4570. https://doi.org/10.1080/01431160110113854
23. Brown J, Tollerud H, Barber C, et al. (2020) Lessons learned implementing an operational continuous United States national land change monitoring capability: The Land Change Monitoring, Assessment, and Projection (LCMAP) approach. *Remote Sens Environ* 238: 111356. https://doi.org/10.1016/j.rse.2019.111356
24. Liu C, Xu X, Feng X, et al. (2023) CALC-2020: a new baseline land cover map at 10 m resolution for the circumpolar Arctic. *Earth Syst Sci Data* 15: 133–153. https://doi.org/10.5194/essd-15-133-2023
25. Ulrich M, Matthes H, Schirrmeister L, et al. (2017) Differences in behavior and distribution of permafrost-related lakes in Central Yakutia and their response to climatic drivers. *Water Resour Res* 53: 1167–1188. https://doi.org/10.1002/2016WR019267
26. Nitze I, Grosse G, Jones B, et al. (2017) Landsat-Based Trend Analysis of Lake Dynamics across Northern Permafrost Regions. *Remote Sens* 9: 640. https://doi.org/10.3390/rs9070640
27. Li L, Zhang X, Li X, et al. (2022) Thermokarst lake changes over the past 40 years in the Qinghai–Tibet Plateau, China. *Front Env Sci* 10: 1051086. https://doi.org/10.3389/fenvs.2022.1051086
28. Yu Y, Hui F, Zhou Y, et al. (2024) The first 10 m resolution thermokarst lake and pond dataset for the Lena Basin in the 2020 thawing season. *Big Earth Data* 8: 302–332. https://doi.org/10.1080/20964471.2023.2280279
29. Qin Y, Zhang C, Lu P (2023) A fully automatic framework for sub-pixel mapping of thermokarst lakes using Sentinel-2 images. *Sci Remote Sen* 8: 100111. https://doi.org/10.1016/j.srs.2023.100111
30. Liu A, Chen Y, Cheng X (2023) Monitoring Thermokarst Lake Drainage Dynamics in Northeast Siberian Coastal Tundra. *Remote Sens* 15, 4396. https://doi.org/10.3390/rs15184396
31. Beck I, Ludwig R, Bernier M, et al. (2015) Assessing Permafrost Degradation and Land Cover Changes (1986–2009) using Remote Sensing Data over Umiujaq, Sub-Arctic Québec. *Permafrost Periglac* 26: 129–141. https://doi.org/10.1002/ppp.1839

32. Boike J, Grau T, Heim B, et al. (2016) Satellite-derived changes in the permafrost landscape of central Yakutia, 2000–2011: Wetting, drying, and fires. *Global Planet Change* 139: 116–127. https://doi.org/10.1016/j.gloplacha.2016.01.001
33. Lee Y, Kim S, Jung Y, et al. (2024) Monitoring Long-Term Land Cover Change in Central Yakutia Using Sparse Time Series Landsat Data. *Remote Sens* 16: 1868. https://doi.org/10.3390/rs16111868
34. Nitze I, Grosse G, Jones B, et al. (2018) Remote sensing quantifies widespread abundance of permafrost region disturbances across the Arctic and Subarctic. *Nat Commun* 9: 5423. https://doi.org/10.1038/s41467-018-07663-3
35. Dubovik O, Schuster G, Xu F, et al. (2021) Grand Challenges in Satellite Remote Sensing. *Front Remote Sens* 2. https://doi.org/10.3389/frsen.2021.619818
36. Gorelick N, Hancher M, Dixon M, et al. (2017) Google Earth Engine: Planetary-scale geospatial analysis for everyone. *Remote Sens Environ* 202: 18–27. https://doi.org/10.1016/j.rse.2017.06.031
37. Amani M, Brisco B, Afshar M, et al. (2019) A generalized supervised classification scheme to produce provincial wetland inventory maps: an application of Google Earth Engine for big geo data processing. *Big Earth Data* 3: 378–394. https://doi.org/10.1080/20964471.2019.1690404
38. Jensen J (2016) *Introductory Digital Image Processing: A Remote Sensing Perspective*, Pearson Education, Incorporated, 623.
39. Talukdar S, Singha P, Mahato S, et al. (2020) Land-Use Land-Cover Classification by Machine Learning Classifiers for Satellite Observations—A Review. *Remote Sens* 12, 1135. https://doi.org/10.3390/rs12071135
40. Zhao Z, Islam F, Waseem LA, et al. (2024) Comparison of Three Machine Learning Algorithms Using Google Earth Engine for Land Use Land Cover Classification. *Rangeland Ecol Manag* 92: 129–137. https://doi.org/10.1016/j.rama.2023.10.007
41. Rawat K, Kumar S, Garg N (2024) Statistical comparison of simple and machine learning based land use and land cover classification algorithms: A case study. *J Water Manag Modell* 32. https://doi.org/10.14796/JWMM.H524
42. Nigar A, Li Y, Jat Baloch M, et al. (2024) Comparison of machine and deep learning algorithms using Google Earth Engine and Python for land classifications. *Front Environ Sci* 12: 1378443. https://doi.org/10.3389/fenvs.2024.1378443
43. Schwamborn G, Rachold V, Grigoriev M (2002) Late Quaternary sedimentation history of the Lena Delta. *Quatern Int* 89: 119–134. https://doi.org/10.1016/S1040-6182(01)00084-2
44. Schwamborn G, Schirrmeister L, Mohammadi A, et al. (2023) Fluvial and permafrost history of the lower Lena River, north-eastern Siberia, over late Quaternary time. *Sedimentology* 70: 235–258. https://doi.org/10.1111/sed.13037
45. Zaplavnova A, Deev E, Potapov V (2024) Structure of the Upper Part of the Earth's Crust in the Area of the Lena River Delta: The First Magnetotelluric Data. *Dokl Earth Sci* 514: 249–254. https://doi.org/10.1134/S1028334X23602833
46. Grigoriev M (1993) *Criomorphogenesis in the Lena Delta*, Yakutsk, Russia: Permafrost Institute Press, 176.
47. Boike J, Nitzbon J, Anders K, et al. (2019) A 16-year record (2002–2017) of permafrost, active-layer, and meteorological conditions at the Samoylov Island Arctic permafrost research site, Lena River delta, northern Siberia: an opportunity to validate remote-sensing data and land surface, snow, and permafrost models. *Earth Syst Sci Data* 11: 261–299. https://doi.org/10.5194/essd-11-261-2019

48. Chalov S, Prokopeva K, Magritsky D, et al. (2023) Climate change impacts on streamflow, sediment load and carbon fluxes in the Lena River delta. *Ecol Indic* 157: 111252. https://doi.org/10.1016/j.ecolind.2023.111252
49. Yurkevich N, Kartoziia A, Tsibizova E (2022) Permafrost degradation impact on water bodies in the Siberian tundra (Samoylov and Kurungnakh Islands, Lena Delta) using GIS analysis of remote sensing data and a geochemical approach. *Water* 14: 2322. https://doi.org/10.3390/w14152322
50. Schwamborn G, Andreev A, Rachold V, et al. (2002) Evolution of Lake Nikolay, Arga Island, Western Lena River Delta, during Late Pleistocene and Holocene Time. *Polarforschung* 70: 69–82. https://doi.org/10013/epic.29859.d001
51. Schirrmeister L, Grosse G, Schwamborn G, et al. (2003) Late Quaternary History of the Accumulation Plain North of the Chekanovsky Ridge (Lena Delta, Russia): A Multidisciplinary Approach. *Polar Geogr* 27: 277–319. https://doi.org/10.1080/789610225
52. Feliks Are, Reimnitz E (2000) An Overview of the Lena River Delta Setting: Geology, Tectonics, Geomorphology, and Hydrology. *J Coastal Res* 16: 1083–1093.
53. Imaeva L, Gusev G, Imaev V (2019) Dynamics of the relief and seismotectonic activity of the modern structures in the delta of the river Lena. *Geotectonics* 5: 62–77. https://doi.org/10.31857/S0016-853X2019562-77
54. Dergach P, Eponeshnikova L, Ponasenko S, et al. (2022) Building a tomographic velocity model for Samoylov Island area (Lena Delta) from local seismological data for the period of 2019–2021. *Geodin tektonofiz* 13: 0627. https://doi.org/10.5800/GT-2022-13-2s-0627
55. Zolnikov I, Glushkova N, Kartoziya A, et al. (2023) The geomorphological zonation of the Lena river delta east part by using GIS-analysis. Geology and Mineral Resources of Siberia 1: 3–11. https://doi.org/10.20403/2078-0575-2023-1-3-11
56. Harmonized Sentinel-2 MSI: MultiSpectral Instrument, Level-2A Available from: https://developers.google.com/earth-engine/datasets/catalog/COPERNICUS_S2_SR_HARMONIZED (accessed on 13 December 2024).
57. Rouse J, Haas R, Deering D, et al. (1973) Monitoring the Vernal Advancement and Retrogradation (Green Wave Effect) of Natural Vegetation. Texas: Remote Sens. Centre, TEXAS A&M Univ., 8.
58. Gao B (1996) NDWI—A normalized difference water index for remote sensing of vegetation liquid water from space. *Remote Sens Environ* 58: 257–266. https://doi.org/10.1016/S0034-4257(96)00067-3
59. Huete A, Didan K, Miura T, et al. (2002) Overview of the radiometric and biophysical performance of the MODIS vegetation indices. *Remote Sens Environ* 83: 195–213. https://doi.org/10.1016/S0034-4257(02)00096-2
60. Kauth R (1976) ThomasG. S., 1976: The tasseled cap – A graphic description of the spectral-temporal development of agricultural crops as seen by Landsat, *Proceedings on the Symposium on Machine Processing of Remotely Sensed Data*, New York: The Institute of Electrical and Electronics Engineers, Inc., 41–51.
61. Shi T, Xu H (2019) Derivation of Tasseled Cap Transformation Coefficients for Sentinel-2 MSI At-Sensor Reflectance Data. *IEEE J Sel Top Appl Earth Observ Remote Sens* 12: 4038–4048. https://doi.org/10.1109/JSTARS.2019.2938388
62. Crist EP, Cicone RC (1984) Application of the tasseled cap concept to simulated thematic mapper data. *Photogramm Eng Remote Sens* 50: 343–352.

63. Kartoziia A (2024) Using Google Earth Engine to Assess the Current State of Thermokarst Terrain on Arga Island (the Lena Delta). *Earth* 5: 228-243. https://doi.org/10.3390/earth5020012
64. Breiman L, Friedman J, Olshen R, et al. (2017) *Classification and regression trees*, New York: Routledge, 368. https://doi.org/10.1201/9781315139470
65. Breiman L (1998) Arcing classifier (with discussion and a rejoinder by the author). *Ann Statist* 26: 1011–1027. https://doi.org/10.1214/aos/1024691079
66. Breiman L (2001) Random Forests. *Mach Learn* 45: 5–32. https://doi.org/10.1023/A:1010933404324
67. Cover T, Hart P (1967) Nearest neighbor pattern classification. *IEEE Trans Inform Theory* 13: 21–27. https://doi.org/10.1109/TIT.1967.1053964
68. Cortes C, Vapnik V (1995) Support-vector networks. *Mach Learn* 20: 273–297. https://doi.org/10.1007/BF00994018
69. Stehman S (1997) Selecting and interpreting measures of thematic classification accuracy. *Remote Sens Environ* 62: 77–89. https://doi.org/10.1016/S0034-4257(97)00083-7
70. Congalton R, Green K (2008) *Assessing the Accuracy of Remotely Sensed Data: Principles and Practices*, Second Edition, Boca Raton: CRC Press, 200. https://doi.org/10.1201/9781420055139
71. Sasaki Y (2007) The truth of the F-measure. *Teach Tutor Mater* 1: 1–5.
72. Cohen J (1960) A Coefficient of Agreement for Nominal Scales. *Educ Psychol Meas* 20: 37–46. https://doi.org/10.1177/001316446002000104
73. Koukoulas S, Blackburn G (2001) Introducing New Indices for Accuracy Evaluation of Classified Images Representing Semi-Natural Woodland Environments. *Photogramm Eng Remote Sens* 67: 499–510.
74. Labatut V, Cherifi H (2011) Evaluation of Performance Measures for Classifiers Comparison. ArXiv abs/1112.4133.
75. Albertz J (2009) *Einführung in die Fernerkundung: Grundlagen der Interpretation von Luft- und Satellitenbildern*, Darmstadt: Wiss. Buchges, 254.
76. Pirotti F, Sunar F, Piragnolo M (2016) Benchmark of machine learning methods for classification of a Sentinel-2 image. *Int. Arch. Photogramm. Remote Sens Spatial Inf Sci* XLI-B7: 335–340. https://doi.org/10.5194/isprs-archives-XLI-B7-335-2016
77. Zhou L, Luo T, Du M, et al. (2021) Machine Learning Comparison and Parameter Setting Methods for the Detection of Dump Sites for Construction and Demolition Waste Using the Google Earth Engine. *Remote Sens* 13. https://doi.org/10.3390/rs13040787
78. Merchant M, Brisco B, Mahdianpari M, et al. (2023) Leveraging Google Earth Engine cloud computing for large-scale arctic wetland mapping. *Int J Appl Earth Obs* 125: 103589. https://doi.org/10.1016/j.jag.2023.103589
79. Nitze I, Grosse G (2016) Detection of landscape dynamics in the Arctic Lena Delta with temporally dense Landsat time-series stacks. *Remote Sens Environ* 181: 27–41. https://doi.org/10.1016/j.rse.2016.03.038